The Astrophysical Journal Letters, 939:L35 (8pp), 2022 November 10 https://doi.org/10.3847/2041-8213/ac8674

A General, Scale-independent Description of the Sound Speed in Neutron Stars

Christian Ecker[1] and Luciano Rezzolla[1,2,3]
[1] Institut für Theoretische Physik, Goethe Universität, Max-von-Laue-Str. 1, D-60438 Frankfurt am Main, Germany; ecker@itp.uni-frankfurt.de
[2] School of Mathematics, Trinity College, Dublin 2, Ireland
[3] Frankfurt Institute for Advanced Studies, Ruth-Moufang-Str. 1, D-60438 Frankfurt am Main, Germany
Received 2022 July 12; revised 2022 July 29; accepted 2022 August 3; published 2022 November 10

Abstract

Using more than a million randomly generated equations of state that satisfy theoretical and observational constraints, we construct a novel, scale-independent description of the sound speed in neutron stars, where the latter is expressed in a unit cube spanning the normalized radius, r/R, and the mass normalized to the maximum one, $M/M_{\rm TOV}$. From this generic representation, a number of interesting and surprising results can be deduced. In particular, we find that light (heavy) stars have stiff (soft) cores and soft (stiff) outer layers, or that the maximum of the sound speed is located at the center of light stars but moves to the outer layers for stars with $M/M_{\rm TOV} \gtrsim 0.7$, reaching a constant value of $c_s^2 = 1/2$ as $M \to M_{\rm TOV}$. We also show that the sound speed decreases below the conformal limit $c_s^2 = 1/3$ at the center of stars with $M = M_{\rm TOV}$. Finally, we construct an analytic expression that accurately describes the radial dependence of the sound speed as a function of the neutron-star mass, thus providing an estimate of the maximum sound speed expected in a neutron star.

Unified Astronomy Thesaurus concepts: Gravitation (661); Fundamental parameters of stars (555); Nuclear astrophysics (1129); Neutron stars (1108); Nuclear physics (2077)

1. Introduction

The extreme conditions in neutron-star interiors pose a formidable problem for the theoretic modeling of nuclear matter several times denser than the saturation density of atomic nuclei, $n_s := 0.16\,\mathrm{fm}^{-3}$. While effective field-theory calculations are arguably the most important tool to obtain theoretical predictions for the behavior of dense matter, the associated uncertainties become large at densities several times n_s, such as those present in neutron-star cores. In addition, first-principle perturbative quantum chromodynamics (QCD) calculations are only reliable at densities much larger than those realized in the neutron-star interior but provide important consistency conditions for the modeling of matter at lower densities (Fraga et al. 2014; Annala et al. 2020, 2022; Gorda et al. 2022; Komoltsev & Kurkela 2022; Somasundaram et al. 2022). Our theoretical control of even basic quantities, such as the equation of state (EOS) of dense nuclear and quark matter that, in the simplest case, is a relation between pressure and the energy density $p(e)$, is therefore still very limited, often forcing the use of agnostic approaches to build the EOS of nuclear matter at neutron-star densities. At the same time, recent and upcoming observations of neutron stars and their merger events represent a unique opportunity to gain information about strongly coupled dense matter under conditions that are either difficult or impossible to create in experiments.

It is therefore important to combine our current theoretical knowledge with the available observational data to make predictions for the EOS and related quantities that determine the macroscopic properties of neutron stars. One such quantity is the (adiabatic) sound speed, which is defined as the derivative of the pressure with respect to the energy density at fixed entropy per baryon s (Rezzolla & Zanotti 2013),

$$c_s^2 := \left(\frac{\partial p}{\partial e}\right)_s. \tag{1}$$

Among its many important properties, the sound speed provides a measure of the stiffness of matter, or in other words, it determines the amount of material pressure available to balance the gravitational pull and therefore prevent a neutron star from collapsing to a black hole. Clearly, a large speed of sound corresponds to a large stiffness, which, in turn, allows for the support of neutron stars with large radii R and large maximum masses $M_{\rm TOV}$. Similarly simple logic would suggest that the sound speed should reach its maximum value in the core of the star.

There exist a number of works (Moustakidis et al. 2017; Tews et al. 2018; Margaritis et al. 2020; Hippert et al. 2021; Kanakis-Pegios et al. 2021; Altiparmak et al. 2022) addressing the question of whether the sound speed as a function of density in QCD has an upper limit that is smaller than the speed of light. One natural conjecture for this bound is the value in conformally symmetric matter, $c_s^2 = 1/3$ (see, e.g., Bedaque & Steiner 2015; Alsing et al. 2018), such as realized in QCD at asymptotically large density. However, it turns out that assuming this conformal limit ($c_s^2 \leqslant 1/3$) strictly at all densities leads to a strong tension with astrophysical measurements of neutron-star masses $M \gtrsim 2\ M_\odot$ (Antoniadis et al. 2013; Cromartie et al. 2019; Fonseca et al. 2021), which favor stiff EOSs with $c_s^2 \gtrsim 1/3$ at densities $\gtrsim n_s$. In addition, various theoretical approaches, such as QCD at large isospin density (Carignano et al. 2017), two-color QCD (Hands et al. 2006), quarkyonic matter (McLerran & Reddy 2019; Duarte et al. 2021; Margueron et al. 2021), models for high-density QCD (Leonhardt et al. 2020; Ma & Rho 2021; Braun & Schallmo 2022; Pal et al. 2022), and models based on the gauge/gravity duality (Ecker et al. 2017; Demircik et al. 2021; Kovensky et al. 2022) predict $c_s^2 > 1/3$ at finite densities.

In other words, there now exists evidence and consensus that the sound speed at neutron-star densities exceeds the conformal limit. However, it still remains unclear what this maximum value should be and, more importantly, where in the neutron-star interior it is achieved. For instance, it is natural to expect that the maximum sound speed should always take place at the center of the star, as this is where the largest densities are achieved. As we will show below, this simple logic is valid for light stars but fails spectacularly as one considers stars near the maximum mass.

In this Letter, we investigate the behavior of the sound speed in the neutron-star interior using input for the EOS from nuclear theory and perturbative QCD and impose observational constraints on neutron-star masses, radii, and tidal deformabilities. Our goal is to make statements that are universal in the sense that they do not depend on a particular choice of the EOS or any of the macroscopic scales, such as the radius and maximum mass of a given EOS. To achieve such a model independence, we randomly generate more than a million EOSs that are by construction consistent with nuclear theory and perturbative QCD at low and high densities, respectively, and satisfy the observational constraints of isolated and binary neutron-star merger measurements. We then generate probability density functions (PDFs) for the sound speed inside nonrotating neutron stars and extract their median and 95% confidence intervals. By choosing dimensionless coordinates for the radial (r/R) and mass dependence ($M/M_{\rm TOV}$), we obtain a novel and entirely scale-independent description of the sound speed in the neutron-star interior.

2. Methods

Our setup is similar to the one presented by Altiparmak et al. (2022), and we briefly review it here. The starting point is the construction of a large number of EOSs, which we achieve by patching together several different components. At the lowest densities, i.e., for $n < 0.5n_s$, we use the Baym–Pethick–Sutherland model (Baym et al. 1971) to describe the neutron-star crust. In the range $0.5n_s < n < 1.1n_s$, we randomly sample polytropes to cover the entire range between the soft and stiff EOSs of Hebeler et al. (2013). At large densities, $\gtrsim 40n_s$, corresponding to a fixed baryon chemical potential of $\mu = 2.6\,\mathrm{GeV}$, we impose the perturbative QCD result of Fraga et al. (2014) for the pressure $p(X, \mu)$ of cold quark matter in terms of a renormalization scale parameter X, which we sample uniformly in the range [1, 4]. Although such high densities are not realized in neutron stars (see, e.g., Altiparmak et al. 2022), imposing $p(X, \mu)$ constrains the EOS at neutron-star densities. Finally, in the intermediate regime of densities, i.e., $1.1n_s < n \lesssim 40n_s$, we use the parameterization method introduced by Annala et al. (2020), which uses a continuous combination of piecewise-linear segments for the sound speed as a function of the chemical potential $c_s^2(\mu)$ as a starting point to construct thermodynamic quantities,

$$c_s^2(\mu) = \frac{(\mu_{i+1} - \mu)c_{s,i}^2 + (\mu - \mu_i)c_{s,i+1}^2}{\mu_{i+1} - \mu_i}, \tag{2}$$

where μ_i and $c_{s,i}^2$ are the parameters of the ith segment in the range $\mu_i \leqslant \mu \leqslant \mu_{i+1}$ (throughout this paper, we use units in which the speed of light and Newton's constant are equal to 1, $c = G = 1$). The number density can then be expressed as

$$n(\mu) = n_1 \exp\left(\int_{\mu_1}^{\mu} \frac{d\mu'}{\mu' c_s^2(\mu')}\right), \tag{3}$$

where $n_1 = 1.1n_s$, and $\mu_1 = \mu(n_1)$ is fixed by the corresponding chemical potential of the polytrope. Integrating Equation (3) then gives the pressure

$$p(\mu) = p_1 + \int_{\mu_1}^{\mu} d\mu' n(\mu'), \tag{4}$$

where the integration constant p_1 is fixed by the pressure of the polytrope at $n = n_1$. We integrate Equation (4) numerically, using a fixed number of seven segments of the form of Equation (2) for the sound speed. Following the procedure above, we construct a large number of EOSs by randomly choosing the maximum speed of sound $c_{s,\max}^2 \in [0, 1]$ and uniformly sample the remaining free coefficients $\mu_i \in [\mu_1, \mu_{N+1}]$, where $\mu_{N+1} = 2.6\,\mathrm{GeV}$, and $c_{s,i}^2 \in [0, c_{s,\max}^2]$ in their respective domains. In this way, we construct 8×10^6 EOSs that are consistent with theoretical uncertainties in nuclear theory and perturbative QCD.

In order to impose constraints provided by the astronomical observations, for each EOS, we solve the Tolman–Oppenheimer–Volkoff (TOV) equations and keep only those EOSs that are consistent with the mass measurements of J0348+0432 (Antoniadis et al. 2013; $M = 2.01 \pm 0.04\,M_\odot$) and J0740+6620 (Cromartie et al. 2019; Fonseca et al. 2021; $M = 2.08 \pm 0.07\,M_\odot$) by rejecting those with maximum mass $M_{\rm TOV} < 2.0\,M_\odot$. In addition, we impose the radius measurements by NICER of J0740+6620 (Miller et al. 2021; Riley et al. 2021) and J0030+0451 (Miller et al. 2019; Riley et al. 2019) by rejecting EOSs with $R < 10.75$ km at $M = 2.0\,M_\odot$ and $R < 10.8$ km at $M = 1.1\,M_\odot$, respectively. Finally, we exploit the detection of GW171817 by LIGO/Virgo to set an upper bound on the binary tidal deformability $\tilde{\Lambda} < 720$ (low-spin priors; the LIGO Scientific Collaboration et al. 2019). Denoting, respectively, with M_i, R_i, and Λ_i the masses, radii, and tidal deformabilities of the binary components, where $\Lambda_i = \frac{2}{3}k_2(R_i/M_i)^5$, $i = 1, 2$, and k_2 is the second tidal Love number, we compute the binary tidal deformability as

$$\tilde{\Lambda} := \frac{16}{13}\frac{(12M_2 + M_1)M_1^4\Lambda_1 + (12M_1 + M_2)M_2^4\Lambda_2}{(M_1 + M_2)^5}. \tag{5}$$

For any choice of $M_{1,2}$ and $R_{1,2}$, we then reject those EOSs with $\tilde{\Lambda} > 720$ for a chirp mass $\mathcal{M}_{\rm chirp} := (M_1M_2)^{3/5}(M_1 + M_2)^{-1/5} = 1.186\,M_\odot$ and $q := M_2/M_1 > 0.73$ as required for consistency with the LIGO/Virgo data for GW170817 (The LIGO Scientific Collaboration et al. 2019). Imposing the observational constraints reduces our original set of 8×10^6 EOSs to $\approx 10^6$ viable EOSs that form the basis for the results presented in the next section.

We note that, in principle, there also exist estimates for the upper bound on the maximum mass $M_{\rm TOV} \lesssim 2.16^{+0.17}_{-0.15}\,M_\odot$ (see Rezzolla et al. 2018 but also Margalit & Metzger 2017; Ruiz et al. 2018; Shibata et al. 2019; Nathanail et al. 2021). However, since this bound requires a number of uncertain model assumptions about the kilonova modeling of GRB 170817A emitted by the merger event GW170817, we do not

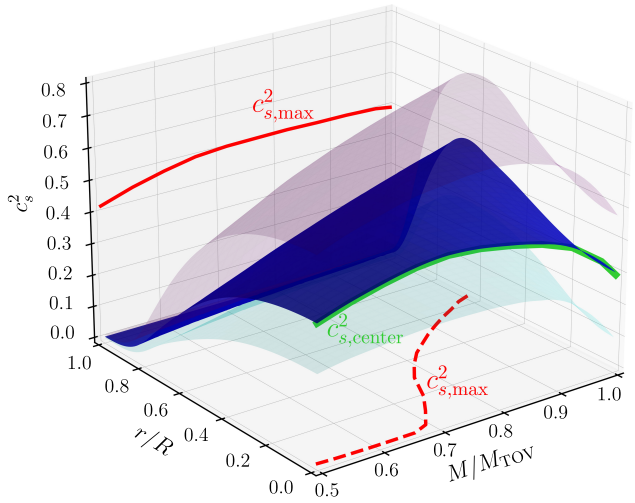

Figure 1. Scale-independent description of the sound speed as a function of the mass M normalized by the maximum mass $M_{\rm TOV}$ and the radial location r normalized by the neutron-star radius R. The blue region represents the median of the PDF, while the cyan and purple regions mark the lower and upper 95% credibility intervals, respectively. Different lines are used to show the important properties of the PDF. The red solid line shows the value of the maximum sound speed, $c^2_{s,\max}$, as a function of the stellar mass, while the red dashed line shows the location within the star of $c^2_{s,\max}$ as a function of the stellar mass; the green solid line reports the sound speed at the stellar center, $c^2_{s,\text{center}}$, as a function of the stellar mass.

impose them on the results presented in the main text but rather study their impact in Appendix A.

3. Results

Figure 1 represents the synthesis and essence of our novel scale-independent representation of the sound speed in neutron stars, which is described in a unit cube having as coordinates the normalized radius $r/R \in [0,\ 1]$, the normalized mass $M/M_{\rm TOV} \in [0,\ 1]$, and the (normalized) sound speed squared $c_s^2 \in [0,\ 1]$ (to aid the visualization of the data, we restrict the unit cube to the most interesting region). In this unit cube, we report with the blue region the median of the sound speed–squared PDF, while the cyan and purple regions mark the 95% credibility intervals.

We first discuss the most prominent global features of the median sound speed. Obviously, close to the surface of the stars ($r/R \approx 1$), the sound speed is small $c_s^2 \sim \mathcal{O}(10^{-2})$ and approximately independent of the mass. This is because the underlying nuclear-theory description at low density is tightly constrained and has a small sound speed. Moving inside the star ($r/R \lesssim 0.8$), the sound speed develops a nontrivial mass dependence. For $M/M_{\rm TOV} \gtrsim 0.7$, the sound speed changes from a monotonic to a nonmonotonic function of r/R that has a single local maximum, $c^2_{s,\max}$, as shown by the red dashed and solid lines in Figure 1. Importantly, the radial location of the maximum sound speed depends on the mass (red dashed line), so that it is at the center of the stars ($r/R = 0$) for light stars ($M/M_{\rm TOV} \lesssim 0.7$) but then moves to the outer layers of the stars ($r/R \simeq 0.5$–0.7) for heavy stars ($M/M_{\rm TOV} \gtrsim 0.7$). This interesting and somewhat surprising behavior highlights how the structure of a compact star depends sensitively on its mass. As we will further discuss below, the value of this local maximum becomes independent of the mass for sufficiently large masses ($M/M_{\rm TOV} \gtrsim 0.7$) and attains a constant value of $c^2_{s,\max} \approx 1/2$ (see also Figure 3). Another important feature of the sound speed is the nonmonotonic behavior of the value at the center of the stars, $c^2_{s,\text{center}}$, as a function of the mass, as shown by the green solid line in Figure 1. Note that the maximum value of $c^2_{s,\text{center}}$ is reached by stars with intermediate mass ($M/M_{\rm TOV} \approx 0.7$), while the minimum value is not obtained in the lightest stars ($M/M_{\rm TOV} = 0.5$) but rather in the heaviest stars ($M/M_{\rm TOV} = 1$), where it is even below the conformal limit, i.e., $c^2_{s,\text{center}} \simeq 0.3$ (see also top right panel of Figure 2).

In Figure 2, we show the PDFs for three different values of the dimensionless mass parameter (top panels) and three values of the mass when expressed in solar masses (bottom panels). In all cases, the red lines represent the median of the PDFs, black solid lines represent the corresponding 95% credibility intervals, and black dashed lines mark the conformal limit $c_s^2 = 1/3$. Note how the red curves clearly show the transition from a monotonic to a nonmonotonic radial dependence of the sound speed when going from light (left) to heavy (right) stars. The sound speed in light stars increases relatively slowly from the surface toward the center, reaching the conformal value only at roughly half its outer radius, i.e., $r/R \approx 0.5$.

As a result, the outer layers of light stars are relatively soft and therefore more sensitive to tidal disruptions than heavier stars. In stars with intermediate mass ($M/M_{\rm TOV} \approx 0.75$), the sound speed increases more rapidly toward the center and remains at a constant value $c_s^2 \approx c^2_{s,\max} = 1/2$ over a large portion ($r/R \lesssim 0.4$) of the core region. Hence, these stars have a relatively large and stiff core compared to lighter ones. Finally, the heaviest stars ($M/M_{\rm TOV} \approx 1$) do not have a sound speed that changes monotonically within the star but, as mentioned above, develop a local maximum rather far from the center ($r/R \approx 0.65$). Hence, heavy stars have relatively soft cores but very stiff outer layers. The stiffening in the outer layers is clearly a consequence of imposing the $2\ M_\odot$ constraint $M_{\rm TOV} > 2\,M_\odot$, while the softening in the core is required to satisfy the perturbative QCD boundary conditions at large densities and, at the same time, maintain causality at all densities. A physically intuitive way of looking at this behavior is the following: as the stellar core softens, the burden of keeping the heavy star stable against gravitational collapse has to be taken by the outer layers, which therefore need to be stiff, i.e., must have large values of the sound speed. Hence, the appearance of a local maximum in the sound speed is a direct consequence of the interplay between the astrophysical constraints ($M_{\rm TOV} \gtrsim 2\,M_\odot$) and the perturbative QCD constraints at high densities.

We note that traditional nuclear-theory EOSs that only capture confined nuclear matter typically do not take into account the perturbative QCD constraints at large densities and therefore cannot lead to the soft core that our statistical approach points out. Indeed, widely used EOSs built on the present understanding of low-density nuclear theory typically predict high-mass stars with cores that are systematically stiffer and therefore with larger sound speeds (see Figure A2 in Appendix B).

The panels in Figure 2 also make it very easy to appreciate that while light and intermediate-mass stars have superconformal central sound speeds ($c^2_{s,\text{center}} > 1/3$; black dashed lines), heavy stars have subconformal central sound speeds ($c^2_{s,\text{center}} < 1/3$), reaching a local minimum of $c^2_{s,\text{center}} \approx 0.3$ for $M/M_{\rm TOV} = 1$.

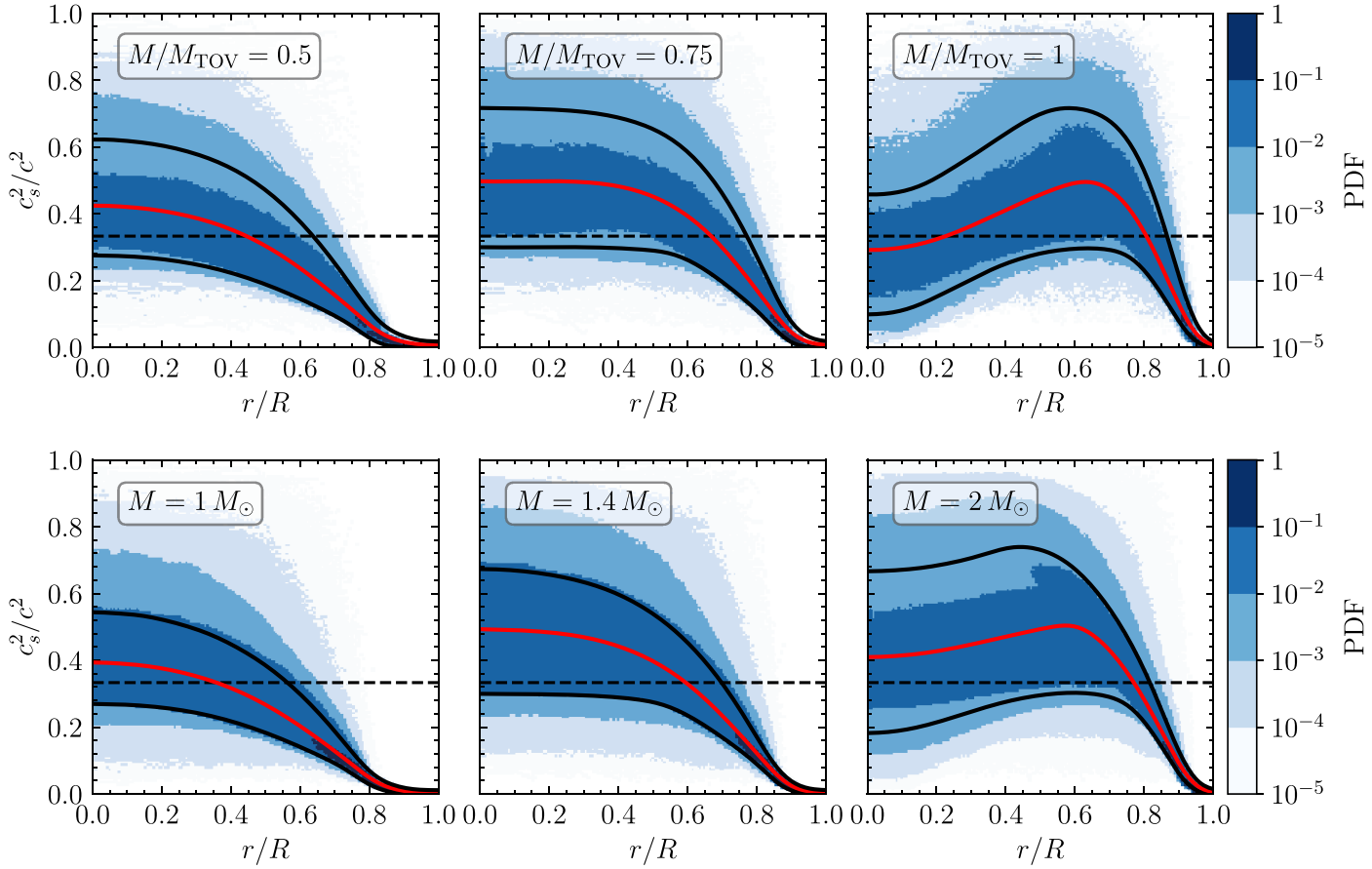

Figure 2. Top panels: PDFs for the sound speed as a function of the normalized radial coordinate r/R for three fixed values of the masses $M = 0.5$ (left), 0.75 (middle), and 1 $M_{\rm TOV}$ (right). Red lines represent the median of the distribution, black solid lines are the upper and lower bounds of the 95% credibility interval, while black dashed lines indicate the conformal limit $c_s^2 = 1/3$. Bottom panels: same as the top panels but shown for representative stellar masses in units of solar mass: $M = 1.0$ (left), 1.4 (middle), and 2.0 $M_\odot$ (right).

Table 1
Numeric Values of the Fitting Parameters in Equation (6) for the Median Sound Speed and the Lower and Upper Bounds of Its 95% Confidence Interval for Three Different Values of $M/M_{\rm TOV}$ Used in Figure 2

$\frac{M}{M_{\rm TOV}}$	Value	α	β	γ	δ	ϵ	ζ	η
	Lower	0.02	0.14	0.47	−12.00	−2.60	15.00	12.00
0.5	Median	0.01	0.21	0.42	−18.00	−1.60	7.70	6.00
	Upper	0.01	0.31	0.37	−27.00	−1.10	6.60	5.00
	Lower	0.09	0.15	0.58	−9.80	−3.40	13.00	11.00
0.75	Median	0.08	0.25	0.55	−10.00	−1.80	9.80	8.40
	Upper	0.09	0.15	0.58	−9.80	−3.40	13.00	11.00
	Lower	0.10	0.03	0.54	−6.40	1.50	14.00	12.00
1	Median	0.18	0.14	0.71	−6.30	−1.50	10.00	8.90
	Upper	0.19	0.23	0.65	−7.80	−0.77	12.00	11.00

The smooth behavior of the medians of the sound speed shown in the panels of Figure 2 encourages the representation of this behavior in terms of analytic functions, namely,

$$c_s^2(x) = (\alpha e^{\beta x^2} + \gamma e^{\delta(x-\epsilon)^2})[1 - \tanh(\zeta x - \eta)], \qquad (6)$$

where $x := r/R$, and $\alpha = 0.18$, $\beta = 0.14$, $\gamma = 0.71$, $\delta = -6.30$, $\epsilon = -1.5$, $\zeta = 10.00$, and $\eta = 8.9$ are the fitting parameters for the most interesting case, namely, the median of the PDF when $M/M_{\rm TOV} = 1$. For completeness, Table 1 in Appendix C reports the values of these coefficients for different mass cuts and credibility intervals.

A few remarks on Equation (6) are in order. First, while these functions are normalized in terms of the stellar radius and maximum mass—none of which are known at present—they nevertheless provide useful information. For instance, notwithstanding the limited knowledge available now, it is already possible to conclude that a neutron star with a mass close to the maximum mass of $\sim 2.2\,M_\odot$ (see, e.g., Rezzolla et al. 2018) and an average radius of ~ 12 km (see, e.g., Altiparmak et al. 2022) will have a maximum sound speed of $c_s \sim 0.7$ at ~ 8 km from the center. This valuable information can already be included in nuclear-theory calculations of new EOSs. Second, although a fit with seven parameters may seem excessive, they are

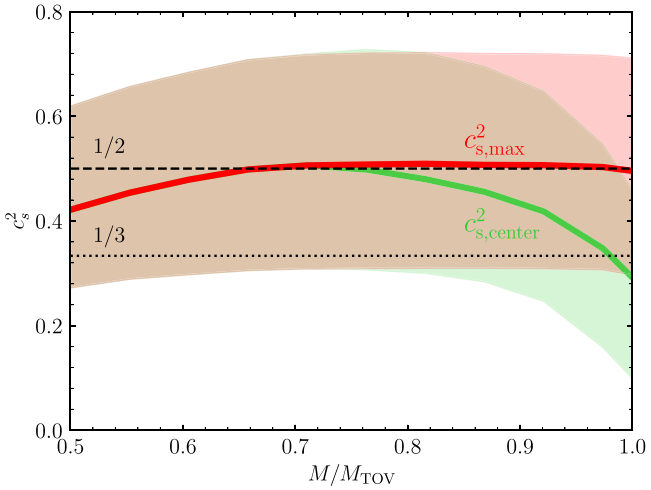

Figure 3. Mass dependence of the median of the local maximum sound speed $c^2_{s,\max}$ (red line) and the sound speed at the neutron-star center $c^2_{s,\rm center}$ (green line); the red and green shaded areas indicate the corresponding 95% credibility intervals. Black dashed and dotted lines mark half the speed of light and the conformal limit, respectively.

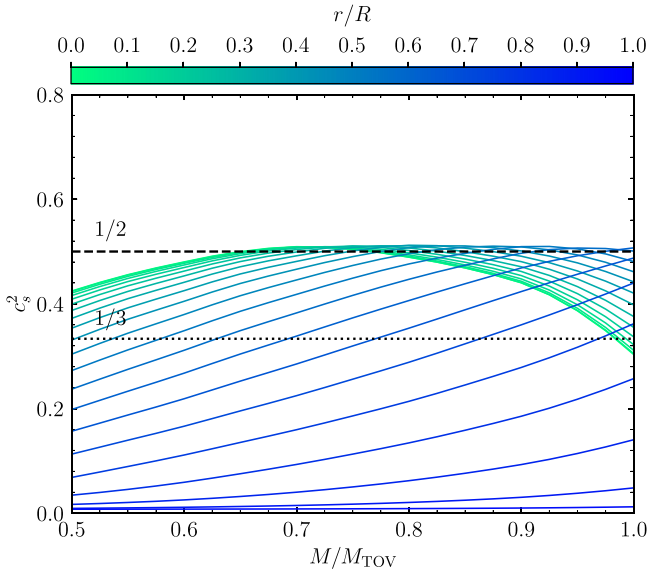

Figure 4. Mass dependence of the median sound speed for various different values of the normalized radial position location inside neutron stars as indicated by the color bar. Black dashed and dotted lines mark half the speed of light and the conformal limit, respectively.

necessary to faithfully represent the key features of the distribution, such as their values at the center ($r=0$) and close to the surface of the stars ($r=R$), as well as the location and value of the local maximum at intermediate radii. Finally, the number of parameters could be reduced by imposing analytic conditions on the approximate behavior of the PDFs in certain limits (e.g., using the vanishing slope at $r/R=0$, 1). However, we have preferred to be conservative and not impose such constraints at the cost of a larger number of parameters.

Figure 3 shows the behavior of the median of the local maximum sound speed $c^2_{s,\max}$ (red line) and the sound speed at the neutron-star center $c^2_{s,\rm center}$ (green line) as a function of the (normalized) stellar mass. The red and green shaded areas indicate the corresponding 95% credibility intervals, while the black dashed and dotted lines mark the values $1/2$ and $1/3$, respectively. In essence, Figure 3 highlights that the maximal sound speed in stars with $M/M_{\rm TOV}\lesssim 0.7$ appears in their center, because the red and green curves coincide for $M/M_{\rm TOV}\lesssim 0.7$. On the other hand, for stars with $M/M_{\rm TOV}\gtrsim 0.7$, the two curves split; the sound speed at the stellar center decreases monotonically toward the stellar interior, reaching a minimum of $c^2_{s,\rm center}\approx 0.3$ for the maximum-mass stars ($M/M_{\rm TOV}=1$). Conversely, the maximum sound remains at a constant value $c^2_{s,\max}\approx 1/2$ for all masses $M/M_{\rm TOV}\lesssim 0.7$. It is suggestive that this constant value is so close to half the speed of light, but it is difficult to invoke any first-principle argument on why this should be the case.

Finally, in Figure 4, we report the behavior of the median of the sound speed as a function of the (normalized) stellar mass at different positions in the star, as indicated by the color bar (these are essentially cuts at different values of r/R of the blue median surface in Figure 1). In particular, the dark green line represents a cut of the median at the stellar center, while the dark blue line shows the behavior at the stellar surface. In essence, Figure 4 highlights how the sound speed changes when going from the surface (dark blue line) toward the core (dark green line) in stars as a function of their mass. At $r/R\approx 0.65$ (light blue line), the sound speed in the heaviest stars reaches its maximum value, $c_s^2\simeq 1/2$, indicated by the black dashed line.

This shows that in the outer layers ($r/R\gtrsim 0.65$) of every star, regardless of its mass, the sound speed is a monotonically increasing function of the mass and has values $c_s^2<1/2$. On the other hand, the sound speed in the core region ($r/R\approx 0$), shown in dark green, is a nonmonotonic function of the neutron-star mass. As a result, the maximum sound speed at the stellar center, i.e., $c^2_{s,\rm center}\approx 1/2$, is not attained in the lightest ($M/M_{\rm TOV}=0.5$) or heaviest ($M/M_{\rm TOV}=1$) stars but rather at intermediate mass, $M/M_{\rm TOV}\approx 0.75$. Furthermore, the sound speed at the center of light stars ($c^2_{s,\rm center}\approx 0.4$) is actually larger than the corresponding value of the heaviest stars ($c^2_{s,\rm center}\approx 0.3$) that, as discussed above, experience a significant softening.

4. Summary and Conclusions

We have studied the sound speed distribution inside neutron stars using a large set of randomly generated EOSs that are consistent with nuclear theory and perturbative QCD results in their respective ranges of validity and in agreement with astrophysical pulsar observations and gravitational-wave detections from binary neutron-star mergers. Our main result is a novel and scale-independent representation of the sound speed in a unit cube spanning the normalized radius r/R and the mass normalized to the maximum one, $M/M_{\rm TOV}$.

This innovative way of thinking about the sound speed has allowed us to draw a number of general conclusions that increase our insight into the quantitative and qualitative behavior in neutron stars of the sound speed in particular and dense nuclear matter in general. More specifically, we find the following.

(i) Close to the surface of the stars, the sound speed is small and approximately independent of the mass. However, moving inside the stars, the sound speed develops a nontrivial mass dependence, and for $M/M_{\rm TOV}\gtrsim 0.7$, it changes from a monotonic to a nonmonotonic function of position r/R with a single local maximum, $c^2_{s,\max}$. The radial location of the maximum sound speed depends on the mass, and it is at the

center of the star for light stars but then moves to the outer layers of the star for heavy stars.

(ii) The value of this local maximum becomes independent of the mass for sufficiently large masses ($M/M_{\rm TOV} \gtrsim 0.7$) and attains a constant value of $c^2_{s,\rm max} \approx 1/2$.

(iii) The sound speed at the center of the stars, $c^2_{s,\rm center}$, also exhibits nonmonotonic behavior as a function of the mass, with the maximum value of $c^2_{s,\rm center}$ being reached by stars with intermediate mass, while the minimum value is not obtained in the lightest stars but rather in the heaviest stars, where it is $c^2_{s,\rm center} \simeq 0.3$ and thus below the conformal limit.

(iv) Using the sound speed as a measure for stiffness, we find that light stars are soft in the outer layers ($r/R \simeq 0.5$–0.7) and stiff in the core, while heavy stars have a soft core and stiff outer layers. This is because the sound speed increases only slowly toward the center in light stars but rapidly in heavy stars, where it approaches a local minimum that is smaller than the conformal limit in the core.

(v) Finally, we provide a simple fitting formula for the median sound speed and its confidence interval in the neutron-star interior. This information can already be included in nuclear-theory calculations of modern EOSs to constrain the behavior of the sound speed in those regions where nuclear-theory predictions have large uncertainties.

In summary, the nontrivial behavior of the sound speed as a function of the radial position inside the stars can be seen as a probe to identify changes of the matter composition. In particular, the softening of heavy neutron-star cores points to the appearance of new degrees of freedom, such as hyperons or deconfined quarks.

There are a number of possible extensions to our work. First, while our method of constructing EOSs includes, in principle, cases that closely resemble a first-order phase transition, they only represent a negligible subset of our ensemble, as we do not explicitly enforce them; hence, their statistical weight is rather small. It would therefore be interesting to include models that, by construction, include a first-order phase transition and study their impact on our results. Second, in the current and also our previous work (Altiparmak et al. 2022), we took the so-called frequentist approach for the statistical interpretation of our results; that is, we impose the constraints with a hard cutoff neglecting their statistical nature. An alternative approach to obtain a statistical interpretation would be a Bayesian analysis, where the statistics of the observational uncertainties is taken into account. Finally, another interesting generalization of our work is its extension to study how rotation—and in particular rapid rotation—affects the properties of the sound speed in neutron stars. We plan to address many of these issues in ongoing and future work.

We thank S. Altiparmak for his contribution in the early stages of this project and R. Duque, E. Fraga, T. Gorda, J. Margueron, C. Moustakidis, and S. Reddy for useful discussions and comments. Partial funding comes from the State of Hesse within the Research Cluster ELEMENTS (Project ID 500/10.006) by the ERC Advanced Grant "JETSET: Launching, propagation and emission of relativistic jets from binary mergers and across mass scales" (grant No. 884631). C.E. acknowledges support by the Deutsche Forschungsgemeinschaft (DFG, German Research Foundation) through the CRC-TR 211 "Strong-interaction matter under extreme conditions"—project No. 315477589—TRR 211. L.R. acknowledges the Walter Greiner Gesellschaft zur Förderung der physikalischen Grundlagenforschung e.V. through the Carl W. Fueck Laureatus Chair. The calculations were performed on the local ITP Supercomputing Clusters Iboga and Calea.

Appendix A
Imposing an Upper Bound on the Maximum Mass

In this Appendix, we analyze the impact on the sound-speed PDF of an additional constraint obtained by imposing an upper bound on the maximum neutron-star mass, namely, $M_{\rm TOV} \lesssim 2.16^{+0.17}_{-0.15}\,M_\odot$, as proposed by Rezzolla et al. (2018; see also Nathanail et al. 2021, for a discussion of the constraints derived from GW190814). Such a constraint is obtained using the detection of the gravitational-wave event GW170817 and the modeling of the kilonova signal of GRB 170817A, together with quasi-universal relations between the maximum masses of uniformly rotating and nonrotating stars (Breu & Rezzolla 2016). Figure A1 shows the sound-speed PDF in a way that is similar to the top panels of Figure 2, with the difference that the PDF here is obtained after imposing an upper limit on the TOV mass $M_{\rm TOV} < 2.16\,M_\odot$. A rapid comparison between Figures A1 and 2 reveals that the overall features of the sound speed remain unchanged. The most significant difference is that the distributions are systematically narrower, simply because the stiff EOSs with large sound speeds are now penalized and rejected. This is particularly clear in the panel for heavy stars (right), where the sound speed increases less rapidly in the outer layers of the star. Interestingly, the value of the local maximum sound speed, $c_{s,\rm max}$, varies only minimally, changing from $c_{s,\rm max} \simeq 1/2$ in the absence of a maximum-mass constraint to $c_{s,\rm max} \simeq 0.45$ when a maximum-mass constraint is imposed.

Appendix B
Comparison to Microphysical Models

In this Appendix, we compare our sound-speed PDF with three microphysical models that have been widely used in the literature to study the properties of neutron stars and their mergers. Figure A2, in particular, compares the radial behavior of the sound-speed PDF in maximally massive stars with the corresponding sound speeds obtained with these EOSs.

The orange line shows the sound speed of a pure nuclear-matter model, the Hempel–Schaffner–Bielich (HS) EOS with DD2 relativistic mean field interactions (Hempel & Schaffner-Bielich 2010; Typel et al. 2010). This EOS is known to be relatively stiff, as can be seen from the large sound speed in the neutron-star interior. Interestingly, for $r/R \gtrsim 0.7$, the sound speed from this EOS agrees very well with the median sound speed (red line) from our approach, even though our construction does not use any input from the (HS)DD2 EOS. However, deeper inside the star, our result is very different from (HS)DD2 and gives less than half the sound speed in the neutron-star core. We should note that the (HS)DD2 EOS gives a relatively high maximum mass of $M_{\rm TOV} \approx 2.5\,M_\odot$ and a tidal deformability of $\Lambda_{1.4} \approx 690$ for $1.4\,M_\odot$ stars, which is in tension with the upper bound $\Lambda_{1.4} \lesssim 580$ derived from the inspiral part (low-spin prior) of GW170817 (The LIGO Scientific Collaboration et al. 2019). This means that (HS) DD2 only provides a good description for dense matter $n \lesssim n_s$ in light stars but is probably too stiff to describe the properties of heavy neutron stars with cores several times denser than n_s.

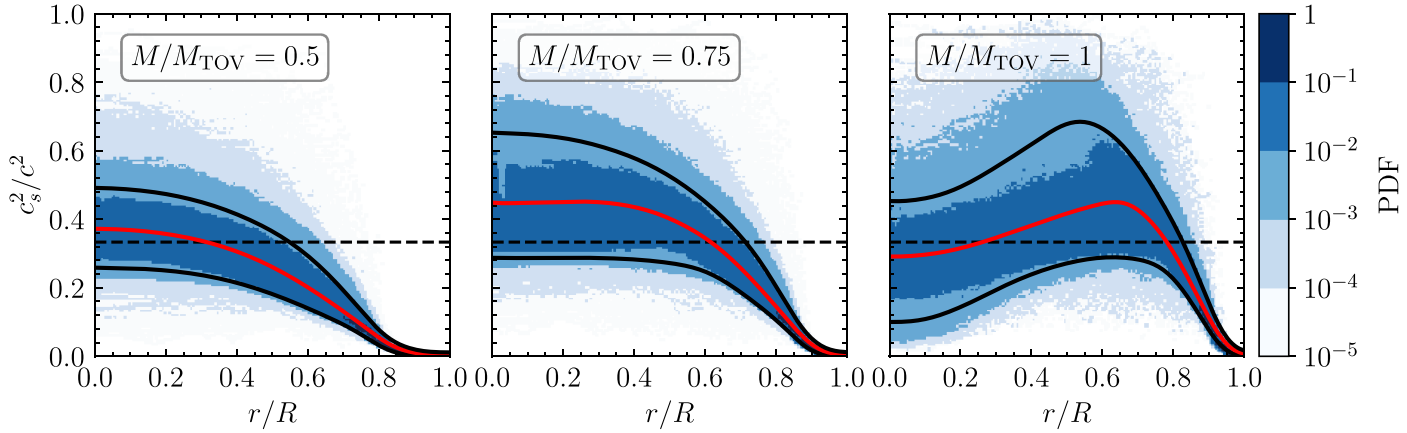

Figure A1. The PDFs for the sound speed as a function of the normalized radial coordinate r/R for three fixed values of the masses $M = 0.5$ (left), 0.75 (middle), and 1 $M_{\rm TOV}$ (right). Red lines represent the median of the distribution, black solid lines are the upper and lower bounds of the 95% credibility interval, and black dashed lines indicates the conformal limit $c_s^2 = 1/3$. This figure is analogous to Figure 2; the only difference is that here an upper limit on the maximum mass $M_{\rm TOV} < 2.16\,M_\odot$ is imposed.

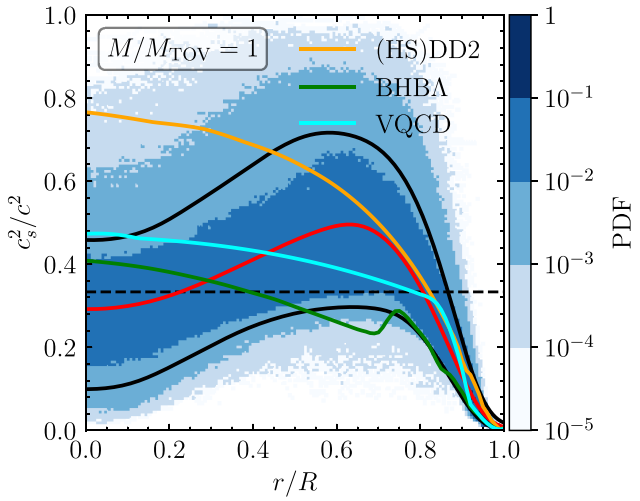

Figure A2. The PDF of the sound speed for $M = M_{\rm TOV}$. The red line represents the median of the distribution, the black solid lines are the upper and lower bounds of the 95% credibility interval, and the black dashed line indicates the conformal limit $c_s^2 = 1/3$. Orange, green, and cyan lines report the cold beta equilibrium sound speed for the HS(DD2) (Hempel & Schaffner-Bielich 2010; Typel et al. 2010), BHBΛ (Banik et al. 2014), and intermediately stiff VQCD (Demircik et al. 2021) EOS, respectively.

The green line, on the other hand, corresponds to the Banik–Hempel–Bandyopadhyay (BHBΛ) EOS (Banik et al. 2014), which is an extension of the (HS)DD2 EOS with Λ hyperons, i.e., particles that contain strange quarks. One of the characteristic features of hyperonic degrees of freedom is that they lead to a softening of the EOS, which can be seen from the local minimum in the sound speed around $r/R \approx 0.8$. The maximum mass of this EOS is relatively low, $M_{\rm TOV} \approx 2.0\,M_\odot$, and therefore in tension with the mass measurement $M \gtrsim 2\,M_\odot$ of heavy pulsars. Hence, the EOS is probably too soft to account for the properties of light stars and the outer layers of heavy stars, as can be seen from the large difference between the red and green curves at $r/R \gtrsim 0.5$ in Figure A2.

Finally, the cyan line corresponds to the intermediately stiff V-QCD EOS of Demircik et al. (2021), which combines the traditional nuclear theory (HS)DD2 and the Akmal–Pandharipande–Ravenhall (Akmal et al. 1998) EOSs at low densities with a string theory–inspired model for QCD to describe dense baryonic and quark matter. This model gives $M_{\rm TOV} = 2.14\,M_\odot$ and $\Lambda_{1.4} = 511$ and therefore conveniently satisfies the 2 $M_\odot$ and tidal deformability constraints. Furthermore, it has recently been verified (Tootle et al. 2022) via binary neutron-star merger simulations that this EOS is not excluded by the expected 1 s long lifetime (Gill et al. 2019) of the postmerger remnant of GW170817. However, although this model passes all currently known theoretical and observational constraints, it is also not able to account for the softening of the core predicted by the red curve.

In summary, none of the three very different microphysical EOSs shown in Figure A2 is able to describe the behavior of the sound speed predicted by our model-agnostic sampling approach. The explanation is simple and reflects the difficulties that nuclear-theory calculations have in matching the high-density, perturbative QCD constraints. It is remarkable that EOSs such as those considered in Figure A2—that are in good agreement with all currently known observational constraints—have radial profiles of the sound speed that are quite different from those predicted from our agnostic approach. This fact shows that the traditional methods of constraining EOS models only with global neutron-star properties such as maximum mass, radii, and tidal deformabilities might not be sufficient. Rather, additional information on the properties inside the stars is needed and can provide further nontrivial constraints. Hence, the importance of our Equation (6) is to provide a novel constraint in terms of the radial distribution of the sound speed inside stars of a given mass. Using this constraint will ensure that the newly suggested EOSs will not only satisfy the astrophysical constraints but also be compatible with the perturbative QCD constraints at much larger densities. We are not aware of a comparable constraint in the literature.

Appendix C
Comprehensive Description of the Fitting

In Table 1, we provide the numerical values of the fitting coefficients for the results shown in Figure 2; these coefficients reflect the astrophysical constraint imposed here of $M_{\rm TOV} \gtrsim 2$ $M_\odot$, and their values may change slightly if this constraint is increased. As briefly mentioned in the main text, some of the parameters in Equation (6) can, in principle, be related by strictly imposing the approximate behavior of the distribution

in certain limits. For example, the numerical results have an approximately vanishing slope at $r/R = 0$, 1, and the value of the local maximum of the median at $0 < r/R < 1$ turns out to be very close to the value $1/2$ in stars with $M/M_{\rm TOV} > 0.7$. Imposing these constraints would allow one to express three of the coefficients in terms of the remaining four but at the same time make the formal Equation (6) more involved. In addition, the upper and lower bounds of the credibility interval do not show the saturation behavior of the local maximum seen in the median such that it would not be possible anymore to express them by the same fitting law. We also remark that the sound speed loses the local maximum for $M/M_{\rm TOV} \lesssim 0.7$ and becomes monotonic, allowing for a simpler fitting law with fewer parameters. This can be directly seen from the values of α provided in Table 1, which become small compared to the other parameters, meaning that the first exponential function in Equation (6) can be neglected, reducing the number of relevant parameters to five.

ORCID iDs

Christian Ecker https://orcid.org/0000-0002-8669-4300
Luciano Rezzolla https://orcid.org/0000-0002-1330-7103

References

Akmal, A., Pandharipande, V. R., & Ravenhall, D. G. 1998, PhRvC, 58, 1804
Alsing, J., Silva, H. O., & Berti, E. 2018, MNRAS, 478, 1377
Altiparmak, S., Ecker, C., & Rezzolla, L. 2022, arXiv:2203.14974
Annala, E., Gorda, T., Katerini, E., et al. 2022, PhRvX, 12, 011058
Annala, E., Gorda, T., Kurkela, A., Nättilä, J., & Vuorinen, A. 2020, NatPh, 16, 907
Antoniadis, J., Freire, P. C. C., Wex, N., et al. 2013, Sci, 340, 6131
Banik, S., Hempel, M., & Bandyopadhyay, D. 2014, ApJS, 214, 22
Baym, G., Pethick, C., & Sutherland, P. 1971, ApJ, 170, 299
Bedaque, P., & Steiner, A. W. 2015, PhRvL, 114, 031103
Braun, J., & Schallmo, B. 2022, arXiv:2204.00358
Breu, C., & Rezzolla, L. 2016, MNRAS, 459, 646
Carignano, S., Lepori, L., Mammarella, A., Mannarelli, M., & Pagliaroli, G. 2017, EPJA, 53, 35
Cromartie, H. T., Fonseca, E., Ransom, S. M., et al. 2019, NatAs, 4, 72
Demircik, T., Ecker, C., & Järvinen, M. 2021, arXiv:2112.12157
Duarte, D. C., Hernandez-Ortiz, S., Jeong, K. S., & McLerran, L. D. 2021, PhRvD, 104, L091901
Ecker, C., Hoyos, C., Jokela, N., Rodríguez Fernández, D., & Vuorinen, A. 2017, JHEP, 11, 031
Fonseca, E., Cromartie, H. T., Pennucci, T .T., et al. 2021, ApJL, 915, L12
Fraga, E. S., Kurkela, A., & Vuorinen, A. 2014, ApJL, 781, L25
Gill, R., Nathanail, A., & Rezzolla, L. 2019, ApJ, 876, 139
Gorda, T., Komoltsev, O., & Kurkela, A. 2022, arXiv:2204.11877
Hands, S., Kim, S., & Skullerud, J.-I. 2006, EPJC, 48, 193
Hebeler, K., Lattimer, J. M., Pethick, C. J., & Schwenk, A. 2013, ApJ, 773, 11
Hempel, M., & Schaffner-Bielich, J. 2010, NuPhA, 837, 210
Hippert, M., Fraga, E. S., & Noronha, J. 2021, PhRvD, 104, 034011
Kanakis-Pegios, A., Koliogiannis, P. S., & Moustakidis, C. C. 2021, Symmetry, 13, 183
Komoltsev, O., & Kurkela, A. 2022, PhRvL, 128, 202701
Kovensky, N., Poole, A., & Schmitt, A. 2022, PhRvD, 105, 034022
Leonhardt, M., Pospiech, M., Schallmo, B., et al. 2020, PhRvL, 125, 142502
Ma, Y.-L., & Rho, M. 2021, arXiv:2104.13822
Margalit, B., & Metzger, B. D. 2017, ApJL, 850, L19
Margaritis, C., Koliogiannis, P. S., & Moustakidis, C. C. 2020, PhRvD, 101, 043023
Margueron, J., Hansen, H., Proust, P., & Chanfray, G. 2021, PhRvC, 104, 055803
McLerran, L., & Reddy, S. 2019, PhRvL, 122, 122701
Miller, M. C., Lamb, F. K, Dittmann., A. J., et al. 2019, ApJL, 887, L24
Miller, M. C., Lamb, F. K., Dittmann, A. J., et al. 2021, ApJL, 918, L28
Moustakidis, C. C., Gaitanos, T., Margaritis, C., & Lalazissis, G. A. 2017, PhRvC, 95, 045801
Nathanail, A., Most, E. R., & Rezzolla, L. 2021, ApJL, 908, L28
Pal, S., Kadam, G., & Bhattacharyya, A. 2022, NuPhA, 1023, 122464
Rezzolla, L., Most, E. R., & Weih, L. R. 2018, ApJL, 852, L25
Rezzolla, L., & Zanotti, O. 2013, Relativistic Hydrodynamics (Oxford: Oxford Univ. Press) 10.1093/acprof:oso/9780198528906.001.0001
Riley, T. E., Watts, A. L., Bogdanov, S., et al. 2019, ApJL, 887, L21
Riley, T. E., Watts, A. L., Ray, P. S., et al. 2021, ApJL, 918, L27
Ruiz, M., Shapiro, S. L., & Tsokaros, A. 2018, PhRvD, 97, 021501
Shibata, M., Zhou, E., Kiuchi, K., & Fujibayashi, S. 2019, PhRvD, 100, 023015
Somasundaram, R., Tews, I., & Margueron, J. 2022, arXiv:2204.14039
Tews, I., Carlson, J., Gandolfi, S., & Reddy, S. 2018, ApJ, 860, 149
The LIGO Scientific Collaborationthe Virgo Collaboration, Abbott, B. P., et al. 2019, PhRvX, 9, 011001
Tootle, S., Ecker, C., Topolski, K., et al. 2022, arXiv:2205.05691
Typel, S., Ropke, G., Klahn, T., Blaschke, D., & Wolter, H. H. 2010, PhRvC, 81, 015803